

Switchable Non-Hermitian Skin Effect in Bogoliubov Modes

Hsuan Lo,¹ You Wang,¹ Rimi Banerjee,¹ Baile Zhang,^{1,2,*} and Y. D. Chong^{1,2,†}

¹*School of Physical and Mathematical Sciences, Nanyang Technological University, Singapore 637371, Singapore*

²*Centre for Disruptive Photonic Technologies, Nanyang Technological University, Singapore, 637371, Singapore*

Interacting or nonlinear lattices can host emergent particle-like modes, such as Bogoliubov quasiparticles, whose band topology and other properties are potentially highly tunable. Despite originating in the study of superconducting materials, Bogoliubov quasiparticles can also occur in synthetic metamaterials. Here, we implement a nonlinear driven-dissipative circuit whose fluctuations are Bogoliubov modes possessing nontrivial non-Hermitian band topology. We show experimentally that the system exhibits a switchable non-Hermitian skin effect (NHSE), which abruptly appears when the on-site driving voltage amplitude exceeds a threshold. In contrast to earlier realizations of the NHSE and related phenomena in circuit models, the switchable NHSE in our system occurs in Bogoliubov modes, which are strongly affected by how the system is driven. Moreover, unlike other experimental platforms hosting non-Hermitian Bogoliubov modes, our system does not contain unconventional asymmetric hopping nonlinearities, only a local Kerr-type nonlinearity.

Introduction—Interacting phases of matter can host various types of emergent quasiparticles, which have the potential to exhibit nontrivial band topology. Such quasiparticles, if they can be reliably produced, may have important implications; for instance, Majorana quasiparticles in topological superconductors [1–4] would enable robust quantum computing [5, 6]. The realization of topological superconductors is a major ongoing challenge in experimental condensed matter physics [4, 7–11], with recent progress in identifying them through the proximity effect [7, 10, 11]. Another way to explore these physical ideas is to use nonlinear synthetic metamaterials. The Bogoliubov-de Gennes (BdG) transformation [12, 13], which gives rise to Bogoliubov quasiparticles in topological superconductors, is also applicable to interacting (i.e., nonlinear) bosonic systems. However, the BdG Hamiltonian for bosonic systems is not guaranteed to be Hermitian [14–18], which implies that the Bogoliubov quasiparticles can have qualitatively different properties, including a broader set of topological phases [19–25]. For example, in exciton-polariton metamaterials [16, 26, 27], it has been predicted [17] that Bogoliubov quasiparticles can exhibit the non-Hermitian skin effect (NHSE), which is related to a form of nontrivial non-Hermitian band topology called point gap winding [24, 28–30]. Such non-Hermitian Bogoliubov modes have only very recently been realised in two experiments, based on optomechanics [31] and superconducting quantum circuits [32], by contrast with the numerous realizations of non-interacting topological phases in linear metamaterials [33].

Here, we report on the experimental implementation of a nonlinear classical circuit metamaterial hosting Bogoliubov quasiparticles with nontrivial non-Hermitian band topology. We uncover a distinctive phenomenon caused by these nonlinear modes: an actively switchable form of the NHSE whereby the intensity profile in a sideband abruptly becomes localized as the driving amplitude increases above a threshold. Our experimental setup

is based on an RLC transmission line [34–42] containing varactors (nonlinear capacitors) [43, 44]. The circuit maps onto a one-dimensional (1D) nonlinear lattice model whose Bogoliubov quasiparticles possess pseudo-Hermiticity [45] and non-Hermitian particle-hole symmetry [22, 46]. Whereas there have been numerous experimental studies of *linear* circuit lattices with various interesting quasiparticles as direct eigenmodes (including non-Hermitian modes exhibiting the NHSE) [38–40, 47–49], the Bogoliubov quasiparticles in our circuit arise through nonlinearity, and are observed as sideband modes away from the fundamental driving frequency. (There have also been experiments on nonlinear circuit lattices in which quasiparticles are generated via higher-harmonic generation, but that is distinct from the Bogoliubov mechanism [50–54].)

The nature of the nonlinearity and the Bogoliubov modes in our system also differs significantly from the previously-mentioned optomechanics and quantum circuit experiments [31, 32], which were both realizations of the “bosonic Kitaev chain” model [55]. In that model, asymmetric pairing processes are engineered into the inter-site couplings, directly causing the Bogoliubov modes to exhibit the NHSE. Our present circuit, however, contains only on-site nonlinearities of the common Kerr type. The Bogoliubov modes exist as fluctuations on a fundamental mode, and their properties can be abruptly switched by changing how that fundamental mode is driven [16, 17]. Specifically, when the circuit’s bulk modes are driven by a low-amplitude voltage, the pseudo-Hermiticity of the Bogoliubov modes is unbroken; but when the amplitude exceeds some threshold, the pseudo-Hermiticity spontaneously breaks [19, 23] and the Bogoliubov spectrum acquires a point gap [24], giving rise to an observable skin effect (localization to one side of the lattice). The circuit itself does not directly contain asymmetric inter-site hoppings, which are often required in linear systems for the emergence of a point gap and the NHSE [28, 29, 40–42]; the asymmetry is imparted by

the fundamental drive. Our work thus establishes an interesting way to create and manipulate non-Hermitian, topologically nontrivial Bogoliubov quasiparticles.

Toy model—Before presenting the experiment, we illustrate its key features using a toy model. Consider a Gross-Pitaevskii equation for two sites $\sigma \in \{0, 1\}$,

$$i \frac{\partial \psi_\sigma}{\partial t} = (\varepsilon - i\gamma)\psi_\sigma + J\psi_{\sigma'} + \frac{g}{2}|\psi_\sigma|^2\psi_\sigma + F_p e^{-i\omega_p t + ik_p \sigma}, \quad (1)$$

where ψ_σ is the complex amplitude, $\sigma' \neq \sigma$ is the opposite site, ε and γ are the on-site frequency and loss, J is the inter-site hopping, and g is a Kerr coefficient. A coherent drive is applied with amplitude F_p , frequency ω_p , and phase difference k_p between the sites.

In the weakly nonlinear regime $g|\psi_\sigma|^2 \ll \varepsilon$, we can apply the BdG transformation [16, 17] by taking the ansatz

$$\psi_\sigma = \left(\Psi e^{ik_p \sigma} + u_\sigma e^{-i\omega_f t} + v_\sigma^* e^{i\omega_f^* t} \right) e^{-i\omega_p t}. \quad (2)$$

Plugging this into (1) yields the eigenproblem

$$\mathbf{H} \begin{pmatrix} \mathbf{u} \\ \mathbf{v} \end{pmatrix} = \tilde{\omega}_f \begin{pmatrix} \mathbf{u} \\ \mathbf{v} \end{pmatrix}, \quad (3)$$

where $\tilde{\omega}_f = \omega_f + i\gamma$, $\mathbf{u} = (u_0, u_1)^T$, $\mathbf{v} = (v_0, v_1)^T$, and

$$\mathbf{H} = \begin{pmatrix} \mathbf{H}_u & \mathbf{H}_v \\ -\mathbf{H}_v^* & -\mathbf{H}_u \end{pmatrix}, \quad (4)$$

$$\mathbf{H}_u = (\varepsilon - \omega_p + g|\Psi|^2)I + J\sigma_1, \quad (5)$$

$$\mathbf{H}_v = \frac{g|\Psi|^2}{4} [(1 + e^{2ik_p})I + (1 - e^{2ik_p})\sigma_3], \quad (6)$$

where I is the 2×2 identity matrix, σ_i is the i -th Pauli matrix, and ω_f is the BdG eigenfrequency. Since \mathbf{H}_v is diagonal, the BdG Hamiltonian \mathbf{H} is manifestly non-Hermitian, with asymmetric couplings between the u (particle) and v (hole) degrees of freedom.

This BdG Hamiltonian obeys a pair of non-Hermitian symmetries [14, 20, 22, 25, 45, 46]: pseudo-Hermiticity, $\mathbf{\Gamma}^3 \mathbf{H} \mathbf{\Gamma}^3 = \mathbf{H}^\dagger$, and non-Hermitian particle-hole (NHPH) symmetry, $\mathbf{\Gamma}^1 \mathbf{H}^* \mathbf{\Gamma}^1 = -\mathbf{H}$, where $\mathbf{\Gamma}^i = \sigma_i \otimes I$. Consequently, the BdG eigenfrequencies form a quadruplet $\{\tilde{\omega}_f, -\tilde{\omega}_f^*, -\tilde{\omega}_f, \tilde{\omega}_f^*\}$ if both symmetries are spontaneously broken, or two pairs $\{\tilde{\omega}_f, -\tilde{\omega}_f\}$ and $\{\tilde{\omega}_f', -\tilde{\omega}_f'\}$ that are purely real (if pseudo-Hermiticity is unbroken) or imaginary (if NHPH symmetry is unbroken). Another consequence is that an eigenstate which spontaneously breaks pseudo-Hermiticity must satisfy $\|\mathbf{u}\|^2 = \|\mathbf{v}\|^2$, where $\|\mathbf{w}\|^2 \equiv \sum_n |w_n|^2$ (see Supplemental Materials [56]). This property, which we call “non-Hermitian particle/hole pinning”, will be useful in the experiment.

Nonlinear circuit—A BdG Hamiltonian of the above form can be realized via the transmission line circuit shown schematically in Fig. 1. This is a 1D lattice of inductively-coupled RLC resonators, each containing a pair of back-to-back varactors that implement a Kerr-like

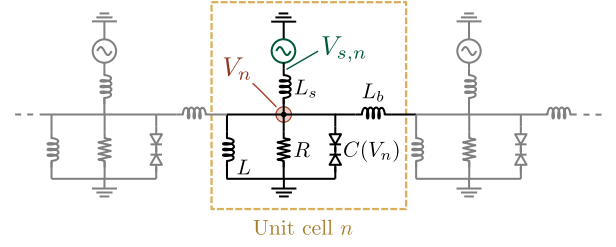


FIG. 1. Design of a driven nonlinear transmission line circuit with a similar BdG Hamiltonian. The dashed box indicates unit cell n . Each unit cell contains a nonlinear capacitance $C(V_n)$ implemented by back-to-back varactors.

nonlinearity [43, 44]. For small voltages ($V \lesssim 1$ V), the nonlinear capacitance has the form $C(V) \approx C_0 + C_1 V^2$. The other transmission line parameters are the on-site resistance R , on-site inductance L , and binding inductance L_b . Each site n is coupled by an inductor L_s to an AC voltage source $V_{s,n} = \frac{1}{2} V_{pp} \sin(\omega_p t + k_p n)$, where V_{pp} and ω_p are tunable and $k_p = 2\pi/3$.

Away from the boundaries, the voltage at resonator n , denoted by V_n , obeys the equation of motion

$$C_0 \ddot{V}_n + \frac{\dot{V}_n}{R} + \left(\frac{1}{L_s} + \frac{2}{L_b} + \frac{1}{L} \right) V_n + C_1 \ddot{V}_n V_n^2 + 2C_1 \dot{V}_n^2 V_n + \frac{1}{L_b} (V_{n+1} + V_{n-1}) + \frac{V_{s,n}}{L_s} = 0. \quad (7)$$

We apply the slowly-varying envelope approximation using the ansatz

$$V_n = \frac{1}{2} (\psi_n(t) e^{-i\omega_p t} + \text{c.c.}), \quad (8)$$

followed by a BdG ansatz for the envelope function:

$$\psi_n(t) = \Psi e^{ik_p n} + u_n e^{-i\omega_f t} + v_n^* e^{i\omega_f^* t}. \quad (9)$$

It can then be shown (see Supplemental Materials [56]) that u_n and v_n obey a BdG eigenproblem. The BdG Hamiltonian has the same form as (4), with \mathbf{H}_u and \mathbf{H}_v expressed in terms of various circuit parameters. For convenience, we will normalize the BdG eigenfrequencies to make them dimensionless, and denote them by Ω_f ; the corresponding physical frequency is $\Omega_f \omega_p - i\gamma$, where γ is a reference decay constant [56]. For a finite lattice under Dirichlet-like or “open” boundary conditions (OBC), the BdG Hamiltonian obeys pseudo-Hermiticity and NHPH symmetry, with the same consequences as in the toy model (with Ω_f replacing $\tilde{\omega}_f$ in the eigenvalue relations). For Floquet-Bloch periodic boundary conditions (PBC) with quasimomentum $k = k_p \neq 0$, pseudo-Hermiticity remains but the NHPH symmetry is explicitly broken.

These properties set the stage for an actively switchable NHSE. In Fig. 2(a), we plot the spectrum of Bogoliubov eigenfrequencies Ω_f for the finite ($N = 30$) lattice under OBC, under different driving voltage amplitudes.

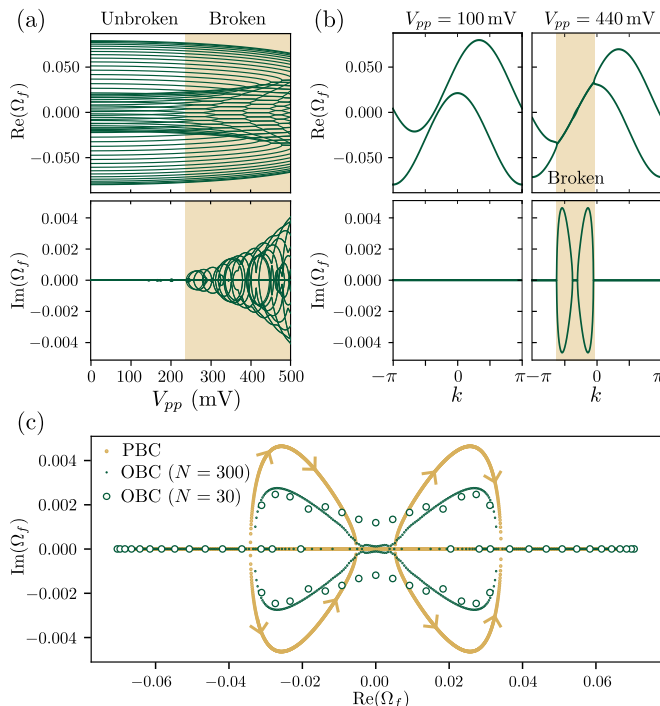


FIG. 2. (a) Bogoliubov eigenfrequency spectrum calculated for the circuit with $N = 30$ unit cells, with OBC, under different driving voltage amplitudes. Pseudo-Hermiticity spontaneously breaks when $V_{pp} \gtrsim 240$ mV. The yellow region indicates the regime of spontaneously broken pseudo-Hermiticity. (b) Bogoliubov band spectrum under PBC for $V_{pp} = 100$ mV (left panels) and $V_{pp} = 440$ mV (right panels). (c) Complex spectra calculated at $V_{pp} = 440$ mV. For the PBC case, each band forms a pair of loops connected by straight segments (yellow curves, with arrows indicating the direction of increasing k as it sweeps from $-\pi$ to π). The eigenfrequencies under OBC (dots: $N = 300$; circles: $N = 30$) deviate markedly from the loop trajectories of the PBC case.

For V_{pp} below around 240 mV, pseudo-Hermiticity is unbroken and all the Ω_f 's are real [19]. As V_{pp} rises above this threshold, pseudo-Hermiticity spontaneously breaks, and the Ω_f 's start becoming non-real; note that we have defined Ω_f so that the physical frequencies have an imaginary shift relative to it; in the experimental regime, the physical frequencies have negative imaginary parts (i.e., the modes are dissipative). The NHPH symmetry is spontaneously broken throughout.

In Fig. 2(b), we plot the complex band spectrum for the Bogoliubov quasiparticles under PBC. There are two bands due to the enlargement of the Hamiltonian under the BdG transformation. In the large V_{pp} regime, we see that the breaking of pseudo-Hermiticity does not occur everywhere in the Brillouin zone, but only a certain range of k . Thus, in the complex Ω_f plane, the spectrum forms the curves plotted in yellow in Fig. 2(c), consisting of two pairs of loops combined with straight segments lying on the real axis. Each band forms a point gapped spectrum (with nonzero winding number ± 1 around any

reference energy within any of the loops) [57]. When the eigenfrequencies of the finite system (under OBC) are plotted in the same graph, we observe that they deviate from the PBC eigenfrequencies, as shown by the dots (for $N = 300$) and circles (for $N = 30$) in Fig. 2(c). These features—point-gap winding under PBC and lack of correspondence with the OBC spectrum—are characteristic of the breakdown of Bloch's theorem and the emergence of the NHSE [24, 28–30].

Results—We implement the transmission line circuit on printed circuit boards (PCBs) such as those shown in Fig. 3(a). The circuit component parameters are $R = 150$ k Ω , $L = L_s = 100$ μ H, $C_0 = 41.34$ pF, $C_1 = -1.649$ pF/V², and $L_b = 1000$ μ H. There are $N = 30$ unit cells, and OBC is implemented by grounding both ends of the transmission line. In the linear ($V_n \approx 0$) regime, each RLC resonator has natural frequency $\omega_0/2\pi = 3.67$ MHz. To apply the fundamental drive, we connect the PCB to three phase-synced function generators, which apply identical sinusoidal voltages of relative phase $\{0, 2\pi/3, 4\pi/3\}$ to sites $n \equiv \{0, 1, 2\} \pmod{3}$, respectively, consistent with the choice of wavenumber $k_p = 2\pi/3$ in the model. To activate the lossy BdG modes, we apply a weaker auxiliary drive at a tunable frequency different from the fundamental drive, with uniform amplitude and phase on all sites (adding phase differences does not substantially affect the results [56]). We then measure the voltage at each site and find its Fourier spectrum.

Fig. 3(b) shows a typical spectrum obtained by the above procedure. Here, we choose $V_{pp} = 500$ mV and $\omega_p/2\pi = 3.81$ MHz for the fundamental drive, so that the system is expected to lie well within the regime of broken pseudo-Hermiticity. For the auxiliary drive, we choose $V'_{pp} = 50$ mV and $\omega'/2\pi = 3.88$ MHz (i.e., normalized sideband frequency $\Omega = (\omega' - \omega_p)/\omega_p = 0.018$). We observe a prominent sideband at precisely the auxiliary drive frequency, as well as a mirror peak on the opposite (undriven) side of the fundamental frequency. The latter is expected due to the mixing between ω_f and $-\omega_f^*$ in the BdG ansatz (9).

We repeat this procedure, changing the site n where the voltage is measured, with all other parameters fixed. In the upper panel of Fig. 3(c), we plot the spatial distribution of the sideband amplitude $V_n^s \equiv \sqrt{|V_n^{\ell}|^2 + |V_n^r|^2}$, where $V_n^{\ell(r)}$ denotes the left (right) sideband voltage amplitude on site n . It is found to be strongly localized to the right of the lattice.

If we probe the lattice at a larger auxiliary drive frequency ($\Omega = 0.058$), the sideband peaks remain observable but their spatial profiles are evenly distributed, as shown in the lower panel of Fig. 3(c). This is related to our previous theoretical finding that only a portion of the modes in the Bogoliubov spectrum may undergo pseudo-Hermiticity breaking [Fig. 2(c)]. A more detailed

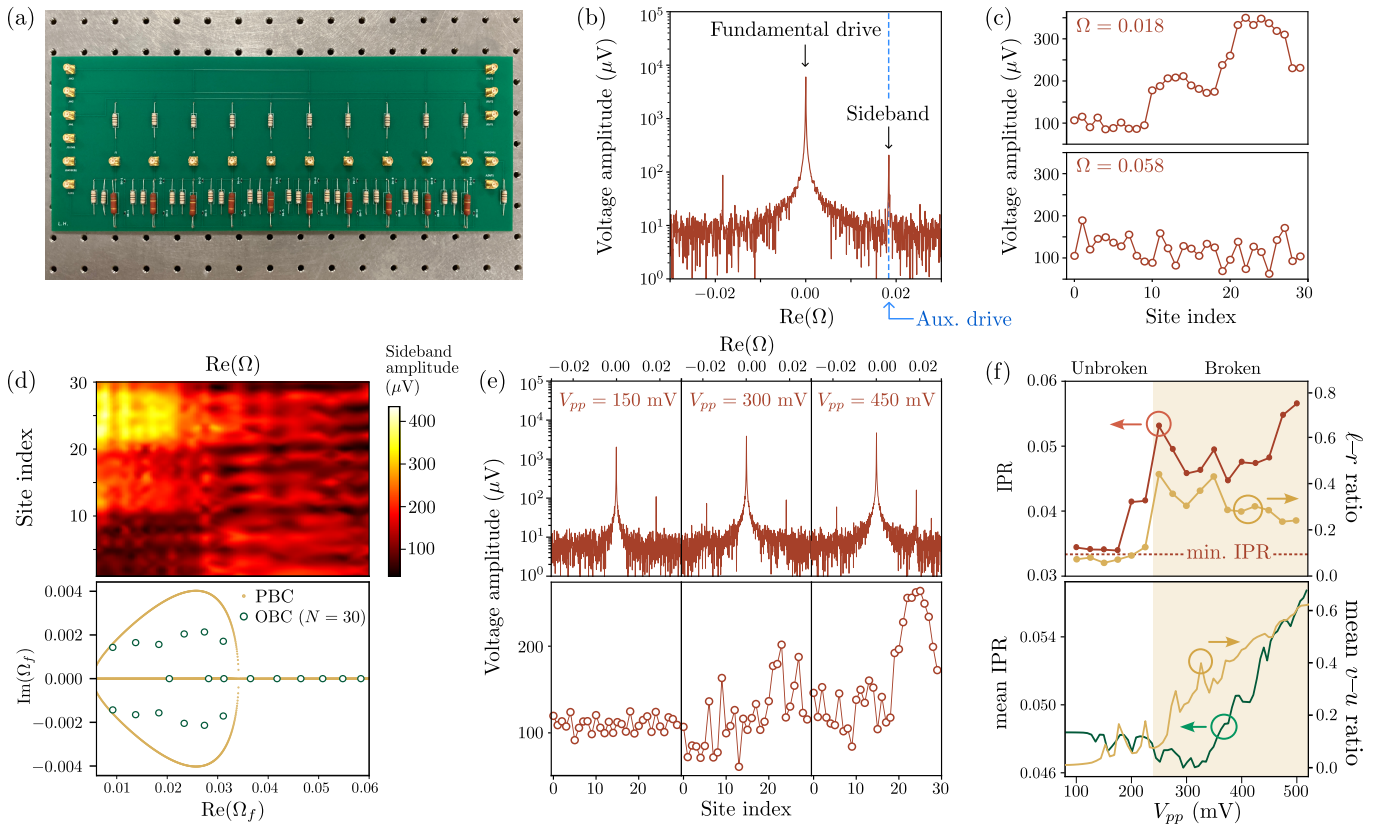


FIG. 3. (a) Circuit implementation of BdG modes with actively switchable NHSE. The sample consists three identical printed circuit boards (PCBs), one of which is shown here, containing 10 sites each. (b) A measured voltage spectrum, at site $n = 30$ for $V_{pp} = 500$ mV. (c) Distribution of sideband voltage amplitudes for $\Omega = 0.018$ (top panel) and $\Omega = 0.058$ (lower panel). The former exhibits strong localization, indicative of the NHSE. (d) Upper panel: sideband amplitude distribution at different auxiliary drive frequencies. Lower panel: calculated Bogoliubov spectra under OBC and PBC. (e) Upper panels: voltage spectra at $n = 30$ for different fundamental drive amplitudes. Lower panels: the corresponding sideband voltage amplitude distributions. (f) Upper panel: experimental results for the inverse participation ratio (IPR, red line) and left-right sideband ratio $\|\mathbf{V}^\ell\|/\|\mathbf{V}^r\|$ (yellow line) versus driving amplitude. Lower panel: theoretical results for the IPR (green line) and particle/hole ratio $\|\mathbf{v}\|/\|\mathbf{u}\|$ (yellow line), averaged over all BdG modes, versus driving amplitude. The yellow-shaded region shows the regime of spontaneously broken pseudo-Hermiticity from Fig. 2(a). In all subplots, the fundamental frequency is $\omega_p/2\pi = 3.81$ MHz and the auxiliary drive amplitude is $V'_{pp} = 50$ mV. In (b) and (e)–(f), the auxiliary drive frequency is fixed at $\omega'/2\pi = 3.88$ MHz, corresponding to $\Omega = 0.018$.

comparison is given in Fig. 3(d): the upper plot shows how the sideband amplitude varies with n and Ω , while the lower panel shows the theoretically-calculated Bogoliubov eigenfrequencies Ω_f . The frequency range where we experimentally observe strong localization is $\Omega \lesssim 0.03$, coincident with the range of $\text{Re}(\Omega_f)$ where the Bogoliubov eigenfrequencies are complex.

Moreover, the NHSE signature is strongly influenced by the driving amplitude. In Fig. 3(e), we plot the measured voltage spectra for three values of V_{pp} (upper panels), and the corresponding sideband spatial profiles (lower panels), at $\Omega = 0.018$. When V_{pp} is small, the NHSE disappears, along with left sideband. In fact, below a critical value of V_{pp} , there is no NHSE for any Ω . Hence, we can use the fundamental drive to perform active switching of the NHSE in the BdG modes.

To illustrate this effect, the upper panel of Fig. 3(f)

shows the effects of V_{pp} , for fixed $\Omega = 0.018$, on (i) the inverse participation ratio $\text{IPR} = \sum_n |V_n^s|^4 / (\sum_m |V_m^s|^2)^2$, a measure of localization [58], and (ii) the amplitude ratio between the left and right sidebands, $\|\mathbf{V}^\ell\|/\|\mathbf{V}^r\|$. As we increase V_{pp} past 240 mV—previously identified in *theory* as the pseudo-Hermiticity breaking point for the finite lattice [Fig. 2(a)]—the experimental results show abrupt increases in the IPR (due to the NHSE) and the sideband amplitude ratio (due to the non-Hermitian particle/hole pinning of the pseudo-Hermiticity-broken BdG eigenstates). These experimental findings are also consistent with the detailed features of the theoretical BdG modes' wavefunctions. In the lower panel of Fig. 3(f), we plot the mean IPR and particle/hole ratio for the BdG modes, which evidently experience similar increases at around the same V_{pp} threshold. Note that the curves

are smoothed out since they are averaged over all BdG modes, and not all BdG modes undergo symmetry breaking simultaneously.

Conclusions—We have experimentally realized a classical nonlinear transmission line that hosts non-Hermitian Bogoliubov quasiparticles. Although there have been numerous demonstrations of tailored quasiparticle modes in linear synthetic metamaterials [27, 33], including circuit lattices [34–36], Bogoliubov quasiparticles [31, 32] are qualitatively different because they are inherently nonlinear. We have demonstrated their ability to host novel phenomena in the form of an actively switchable non-Hermitian skin effect, caused by the interplay between nonlinearity and spontaneous non-Hermitian symmetry breaking [19, 25]. In the future, it would be interesting to use such methods to realize Bogoliubov quasiparticles that belong to other non-Hermitian topological classes [22], which could exhibit more complex, and potentially useful, behaviors.

This work was supported by the Singapore National Research Foundation (NRF) under NRF Investigatorship NRF-NRFI08-2022-0001 and Competitive Research Program (CRP) NRF-CRP23-2019-0005, NRF-CRP23-2019-0007, and NRF-CRP29-2022-0003.

* blzhang@ntu.edu.sg

† yidong@ntu.edu.sg

- [1] J. Alicea, New directions in the pursuit of majorana fermions in solid state systems, *Reports on progress in physics* **75**, 076501 (2012).
- [2] C. Beenakker, Search for majorana fermions in superconductors, *Annu. Rev. Condens. Matter Phys.* **4**, 113 (2013).
- [3] M. Sato and S. Fujimoto, Majorana fermions and topology in superconductors, *Journal of the Physical Society of Japan* **85**, 072001 (2016).
- [4] M. Sato and Y. Ando, Topological superconductors: a review, *Reports on Progress in Physics* **80**, 076501 (2017).
- [5] D. Aasen, M. Hell, R. V. Mishmash, A. Higginbotham, J. Danon, M. Leijnse, T. S. Jespersen, J. A. Folk, C. M. Marcus, K. Flensberg, *et al.*, Milestones toward majorana-based quantum computing, *Physical Review X* **6**, 031016 (2016).
- [6] S. D. Sarma, M. Freedman, and C. Nayak, Majorana zero modes and topological quantum computation, *npj Quantum Information* **1**, 1 (2015).
- [7] L. Fu and C. L. Kane, Superconducting proximity effect and majorana fermions at the surface of a topological insulator, *Phys. Rev. Lett.* **100**, 096407 (2008).
- [8] M. Leijnse and K. Flensberg, Introduction to topological superconductivity and majorana fermions, *Semiconductor Science and Technology* **27**, 124003 (2012).
- [9] P. Zhang, K. Yaji, T. Hashimoto, Y. Ota, T. Kondo, K. Okazaki, Z. Wang, J. Wen, G. D. Gu, H. Ding, *et al.*, Observation of topological superconductivity on the surface of an iron-based superconductor, *Science* **360**, 182 (2018).
- [10] S. Frolov, M. Manfra, and J. Sau, Topological superconductivity in hybrid devices, *Nature Physics* **16**, 718 (2020).
- [11] C. Trang, N. Shimamura, K. Nakayama, S. Souma, K. Sugawara, I. Watanabe, K. Yamauchi, T. Oguchi, K. Segawa, T. Takahashi, *et al.*, Conversion of a conventional superconductor into a topological superconductor by topological proximity effect, *Nature communications* **11**, 159 (2020).
- [12] N. Bogoliubov, On the theory of superfluidity, *J. Phys* **11**, 23 (1947).
- [13] J.-X. Zhu, *Bogoliubov-de Gennes method and its applications*, Vol. 924 (Springer, 2016).
- [14] S. Lieu, Topological symmetry classes for non-hermitian models and connections to the bosonic bogoliubov–de gennes equation, *Physical Review B* **98**, 115135 (2018).
- [15] A. McDonald, T. Pereg-Barnea, and A. A. Clerk, Phase-dependent chiral transport and effective non-hermitian dynamics in a bosonic kitaev-majorana chain, *Phys. Rev. X* **8**, 041031 (2018).
- [16] R. Banerjee, S. Mandal, and T. Liew, Coupling between exciton-polariton corner modes through edge states, *Physical Review Letters* **124**, 063901 (2020).
- [17] X. Xu, H. Xu, S. Mandal, R. Banerjee, S. Ghosh, and T. C. H. Liew, Interaction-induced double-sided skin effect in an exciton-polariton system, *Physical Review B* **103**, 235306 (2021).
- [18] Q. Wang, C. Zhu, Y. Wang, B. Zhang, and Y. D. Chong, Amplification of quantum signals by the non-hermitian skin effect, *Phys. Rev. B* **106**, 024301 (2022).
- [19] C. M. Bender, Making sense of non-hermitian hamiltonians, *Reports on Progress in Physics* **70**, 947 (2007).
- [20] Y. Nakamura, M. Mine, M. Okumura, and Y. Yamanaoka, Condition for emergence of complex eigenvalues in the bogoliubov–de gennes equations, *Physical Review A—Atomic, Molecular, and Optical Physics* **77**, 043601 (2008).
- [21] Y. Kawaguchi and M. Ueda, Spinor bose–einstein condensates, *Physics Reports* **520**, 253 (2012).
- [22] K. Kawabata, K. Shiozaki, M. Ueda, and M. Sato, Symmetry and topology in non-hermitian physics, *Physical Review X* **9**, 041015 (2019).
- [23] Y. Ashida, Z. Gong, and M. Ueda, Non-hermitian physics, *Advances in Physics* **69**, 249 (2020).
- [24] E. J. Bergholtz, J. C. Budich, and F. K. Kunst, Exceptional topology of non-hermitian systems, *Reviews of Modern Physics* **93**, 015005 (2021).
- [25] Q. Wang and Y. D. Chong, Non-hermitian photonic lattices: tutorial, *J. Opt. Soc. Am. B* **40**, 1443 (2023).
- [26] H. Deng, H. Haug, and Y. Yamamoto, Exciton-polariton bose-einstein condensation, *Rev. Mod. Phys.* **82**, 1489 (2010).
- [27] I. Carusotto and C. Ciuti, Quantum fluids of light, *Rev. Mod. Phys.* **85**, 299 (2013).
- [28] N. Hatano and D. R. Nelson, Localization transitions in non-hermitian quantum mechanics, *Physical review letters* **77**, 570 (1996).
- [29] S. Yao and Z. Wang, Edge states and topological invariants of non-hermitian systems, *Physical review letters* **121**, 086803 (2018).
- [30] X. Zhang, T. Zhang, M.-H. Lu, and Y.-F. Chen, A review on non-hermitian skin effect, *Advances in Physics: X* **7**, 2109431 (2022).
- [31] J. J. Slim, C. C. Wanjura, M. Brunelli, J. Del Pino,

- A. Nunnenkamp, and E. Verhagen, Optomechanical realization of the bosonic kitaev chain, *Nature* **627**, 767 (2024).
- [32] J. H. Busnaina, Z. Shi, A. McDonald, D. Dubyna, I. Nsanzineza, J. S. Hung, C. S. Chang, A. A. Clerk, and C. M. Wilson, Quantum simulation of the bosonic kitaev chain, *Nature Communications* **15**, 3065 (2024).
- [33] T. Ozawa, H. M. Price, A. Amo, N. Goldman, M. Hafezi, L. Lu, M. C. Rechtsman, D. Schuster, J. Simon, O. Zilberberg, and I. Carusotto, Topological photonics, *Rev. Mod. Phys.* **91**, 015006 (2019).
- [34] V. V. Albert, L. I. Glazman, and L. Jiang, Topological properties of linear circuit lattices, *Physical review letters* **114**, 173902 (2015).
- [35] J. Ningyuan, C. Owens, A. Sommer, D. Schuster, and J. Simon, Time-and site-resolved dynamics in a topological circuit, *Physical Review X* **5**, 021031 (2015).
- [36] C. H. Lee, S. Imhof, C. Berger, F. Bayer, J. Brehm, L. W. Molenkamp, T. Kiessling, and R. Thomale, Topoelectrical circuits, *Communications Physics* **1**, 39 (2018).
- [37] S. Imhof, C. Berger, F. Bayer, J. Brehm, L. W. Molenkamp, T. Kiessling, F. Schindler, C. H. Lee, M. Greiter, T. Neupert, *et al.*, Topoelectrical-circuit realization of topological corner modes, *Nature Physics* **14**, 925 (2018).
- [38] M. Ezawa, Electric circuits for non-hermitian chern insulators, *Physical Review B* **100**, 081401 (2019).
- [39] T. Hofmann, T. Helbig, C. H. Lee, M. Greiter, and R. Thomale, Chiral voltage propagation and calibration in a topoelectrical chern circuit, *Physical review letters* **122**, 247702 (2019).
- [40] T. Helbig, T. Hofmann, S. Imhof, M. Abdelghany, T. Kiessling, L. Molenkamp, C. Lee, A. Szameit, M. Greiter, and R. Thomale, Generalized bulk–boundary correspondence in non-hermitian topoelectrical circuits, *Nature Physics* **16**, 747 (2020).
- [41] T. Hofmann, T. Helbig, F. Schindler, N. Salgo, M. Brzezińska, M. Greiter, T. Kiessling, D. Wolf, A. Vollhardt, A. Kabaši, *et al.*, Reciprocal skin effect and its realization in a topoelectrical circuit, *Physical review research* **2**, 023265 (2020).
- [42] S. Liu, R. Shao, S. Ma, L. Zhang, O. You, H. Wu, Y. J. Xiang, T. J. Cui, and S. Zhang, Non-hermitian skin effect in a non-hermitian electrical circuit, *Research* (2021).
- [43] Y. Hadad, J. C. Soric, A. B. Khanikaev, and A. Alu, Self-induced topological protection in nonlinear circuit arrays, *Nature Electronics* **1**, 178 (2018).
- [44] Y. Wang, L.-J. Lang, C. H. Lee, B. Zhang, and Y. Chong, Topologically enhanced harmonic generation in a nonlinear transmission line metamaterial, *Nature communications* **10**, 1102 (2019).
- [45] A. Mostafazadeh, Pseudo-hermiticity versus pt symmetry: The necessary condition for the reality of the spectrum of a non-hermitian hamiltonian, *Journal of Mathematical Physics* **43**, 205 (2002).
- [46] A. P. Schnyder, S. Ryu, A. Furusaki, and A. W. Ludwig, Classification of topological insulators and superconductors in three spatial dimensions, *Physical Review B—Condensed Matter and Materials Physics* **78**, 195125 (2008).
- [47] K. Luo, J. Feng, Y. Zhao, and R. Yu, Nodal manifolds bounded by exceptional points on non-hermitian honeycomb lattices and electrical-circuit realizations, *arXiv preprint arXiv:1810.09231* (2018).
- [48] S. Liu, S. Ma, C. Yang, L. Zhang, W. Gao, Y. J. Xiang, T. J. Cui, and S. Zhang, Gain-and loss-induced topological insulating phase in a non-hermitian electrical circuit, *Physical Review Applied* **13**, 014047 (2020).
- [49] X.-X. Zhang and M. Franz, Non-hermitian exceptional landau quantization in electric circuits, *Physical Review Letters* **124**, 046401 (2020).
- [50] A. V. Buryak and Y. S. Kivshar, Solitons due to second harmonic generation, *Physics Letters A* **197**, 407 (1995).
- [51] I. V. Shadrivov, A. A. Zharov, and Y. S. Kivshar, Second-harmonic generation in nonlinear left-handed metamaterials, *JOSA B* **23**, 529 (2006).
- [52] I. V. Shadrivov, A. B. Kozyrev, D. W. van der Weide, and Y. S. Kivshar, Tunable transmission and harmonic generation in nonlinear metamaterials, *Applied Physics Letters* **93** (2008).
- [53] Y. Wang, L.-J. Lang, C. H. Lee, B. Zhang, and Y. D. Chong, Topologically enhanced harmonic generation in a nonlinear transmission line metamaterial, *Nature Communications* **10**, 1102 (2019).
- [54] D. Smirnova, S. Kruk, D. Leykam, E. Melik-Gaykazyan, D.-Y. Choi, and Y. Kivshar, Third-harmonic generation in photonic topological metasurfaces, *Physical review letters* **123**, 103901 (2019).
- [55] A. McDonald, T. Pereg-Barnea, and A. Clerk, Phase-dependent chiral transport and effective non-hermitian dynamics in a bosonic kitaev-majorana chain, *Physical Review X* **8**, 041031 (2018).
- [56] See online Supplemental Materials.
- [57] K. Zhang, Z. Yang, and C. Fang, Correspondence between winding numbers and skin modes in non-hermitian systems, *Physical Review Letters* **125**, 126402 (2020).
- [58] D. J. Thouless, Electrons in disordered systems and the theory of localization, *Phys. Rep.* **13**, 93 (1974).

Supplemental Materials for

“Observation of Non-Hermitian Skin Effect in Bogoliubov Modes”

TWO-SITE TOY MODEL

In this section, we provide a more detailed description of the nonlinear toy model described in the main text. This is a tight-binding model with two sites $\sigma \in \{0, 1\}$. Each site has the same on-site energy ε , linear loss $-i\gamma$, and Kerr-type nonlinearity $g|\psi_n|^2\psi_n$. The coupling J is symmetric (i.e., reciprocal). A drive $F_p e^{-i\omega_p t + ik_p \sigma}$ is applied, with the same amplitude but with a phase shift of k_p between the two sites. The system is described by a set of Gross-Pitaevskii equations (with \hbar omitted):

$$i\frac{\partial\psi_0}{\partial t} = (\varepsilon - i\gamma)\psi_0 + J\psi_1 + \frac{1}{2}g|\psi_0|^2\psi_0 + F_p e^{-i\omega_p t}, \quad (\text{S1})$$

$$i\frac{\partial\psi_1}{\partial t} = (\varepsilon - i\gamma)\psi_1 + J\psi_0 + \frac{1}{2}g|\psi_1|^2\psi_1 + F_p e^{-i\omega_p t + ik_p}. \quad (\text{S2})$$

Firstly, let us define the envelope function $\Phi_\sigma(t)$ by

$$\psi_\sigma = \Phi_\sigma(t) e^{-i\omega_p t}, \quad (\text{S3})$$

which allows us to re-express Eqs. (S1)–(S2) as

$$i\dot{\Phi}_\sigma + \omega_p \Phi_\sigma = (\varepsilon - i\gamma)\Phi_\sigma + J\Phi_{\sigma'} + \frac{1}{2}g|\Phi_\sigma|^2\Phi_\sigma + F_p e^{i\sigma k_p}. \quad (\text{S4})$$

Then we use the BdG transformation to formulate the ansatz

$$\Phi_\sigma(t) = \Psi_\sigma + u_\sigma e^{-i\omega_f t} + v_\sigma^* e^{i\omega_f^* t}, \quad (\text{S5})$$

where Ψ_σ is the steady state amplitude, and u_σ and v_σ are the BdG quasiparticle/quasihole amplitudes. We let $g|\psi_\sigma|^2 \ll \varepsilon$, so that $|u_\sigma|, |v_\sigma| \ll |\Psi|$ and $\omega_f \ll \omega_p$. For ease of presentation, let us also define the time-dependent BdG amplitudes

$$\mu_\sigma(t) = u_\sigma e^{-i\omega_f t}, \quad (\text{S6})$$

$$\nu_\sigma(t) = v_\sigma e^{-i\omega_f t}. \quad (\text{S7})$$

Thus, the time derivative of (S5) is

$$\dot{\Phi}_\sigma = -i\omega_f \mu_\sigma(t) + i\omega_f^* \nu_\sigma^*(t), \quad (\text{S8})$$

and the absolute square of (S5) can be written as

$$|\Phi_\sigma|^2 = (\Psi_\sigma + \mu_\sigma + \nu_\sigma^*)(\Psi_\sigma^* + \mu_\sigma^* + \nu_\sigma) \quad (\text{S9})$$

$$= |\Psi_\sigma|^2 + \Psi_\sigma \mu_\sigma^* + \Psi_\sigma \nu_\sigma + \Psi_\sigma^* \mu_\sigma + \Psi_\sigma^* \nu_\sigma^*. \quad (\text{S10})$$

We now plug the ansatz (S5), as well as the intermediate results (S8) and (S10), into Eq. (S4). During this procedure, we discard terms involving second- and higher-order BdG amplitudes, such as $|\mu_\sigma|^2$ and $|\nu_\sigma|^2$. This yields an equation of the form

$$(\dots) + (\dots)e^{-i\omega_f t} + (\dots)e^{i\omega_f^* t} = 0.$$

We collect the terms with different time dependences—i.e., the time-independent terms, those that go as $e^{-i\omega_f t}$, and those that go as $e^{i\omega_f^* t}$ —separately, resulting in the following set of three equations:

$$\omega_p \Psi_\sigma = (\varepsilon - i\gamma)\Psi_\sigma + J\Psi_{\sigma'} + \frac{1}{2}g|\Psi_\sigma|^2\Psi_\sigma + F_p e^{i\sigma k_p} \quad (\text{S11})$$

$$\omega_f u_\sigma + \omega_p u_\sigma = (\varepsilon - i\gamma)u_\sigma + J u_{\sigma'} + \frac{1}{2}g(2|\Psi_\sigma|^2 u_\sigma + \Psi_\sigma^2 v_\sigma), \quad (\text{S12})$$

$$-\omega_f v_\sigma + \omega_p v_\sigma = (\varepsilon + i\gamma)v_\sigma + J v_{\sigma'} + \frac{1}{2}g(2|\Psi_\sigma|^2 v_\sigma + (\Psi_\sigma^2)^* u_\sigma). \quad (\text{S13})$$

We solve Eq. (S11) by taking $\Psi_\sigma = \Psi e^{ik_p\sigma}$. The remaining equations, (S12)–(S13), can then be organized into the eigenproblem

$$\begin{pmatrix} \varepsilon - \omega_p + g|\Psi|^2 & J & \frac{1}{2}g|\Psi|^2 & 0 \\ J & \varepsilon - \omega_p + g|\Psi|^2 & 0 & \frac{1}{2}g|\Psi|^2 e^{2ik_p} \\ -\frac{1}{2}g|\Psi|^2 & 0 & -\varepsilon + \omega_p - g|\Psi|^2 & -J \\ 0 & -\frac{1}{2}g|\Psi|^2 e^{-2ik_p} & -J & -\varepsilon + \omega_p - g|\Psi|^2 \end{pmatrix} \begin{pmatrix} u_1 \\ u_2 \\ v_1 \\ v_2 \end{pmatrix} = \tilde{\omega}_f \begin{pmatrix} u_1 \\ u_2 \\ v_1 \\ v_2 \end{pmatrix}, \quad (\text{S14})$$

where

$$\tilde{\omega}_f = \omega_f + i\gamma. \quad (\text{S15})$$

The matrix on the left side of (S14) is the Bogoliubov Hamiltonian \mathbf{H} . It has the form

$$\mathbf{H} = \begin{pmatrix} \mathbf{H}_u & \mathbf{H}_v \\ -\mathbf{H}_v^* & -\mathbf{H}_u \end{pmatrix}, \quad (\text{S16})$$

$$\mathbf{H}_u = (\varepsilon - \omega_p + g|\Psi|^2)I_{2 \times 2} + J\sigma_1, \quad (\text{S17})$$

$$\mathbf{H}_v = \frac{g|\Psi|^2}{4} [(1 + e^{2ik_p})I + (1 - e^{2ik_p})\sigma_3]. \quad (\text{S18})$$

Here, σ_i denotes the i -th Pauli matrix and I is the identity matrix.

SYMMETRIES OF THE BDG HAMILTONIAN

The Hamiltonian (S16) has two notable symmetries. The first is the non-Hermitian particle-hole (NHPH) symmetry

$$\{\mathbf{H}, \Gamma^1 \mathbf{K}\} = 0, \quad (\text{S19})$$

where

$$\Gamma^1 = \begin{pmatrix} \mathbf{0} & \mathbf{I} \\ \mathbf{I} & \mathbf{0} \end{pmatrix} \quad (\text{S20})$$

and \mathbf{K} is the complex conjugation operator. This symmetry implies that if φ is an eigenvector of \mathbf{H} with eigenvalue $\tilde{\omega}_f$, then

$$\mathbf{H}(\Gamma^1 \mathbf{K}\varphi) = -\Gamma^1 \mathbf{K}(\mathbf{H}\varphi) = -\tilde{\omega}_f^*(\Gamma^1 \mathbf{K}\varphi). \quad (\text{S21})$$

Therefore, $\Gamma^1 \mathbf{K}\varphi$ is an eigenvector with eigenvalue $-\tilde{\omega}_f^*$.

The second symmetry is pseudo-Hermiticity:

$$\Gamma^3 \mathbf{H} \Gamma^3 = \mathbf{H}^\dagger, \quad (\text{S22})$$

where

$$\Gamma^3 = \begin{pmatrix} \mathbf{I} & \mathbf{0} \\ \mathbf{0} & -\mathbf{I} \end{pmatrix}. \quad (\text{S23})$$

This symmetry implies that if φ is a (right) eigenvector of \mathbf{H} with eigenvalue $\tilde{\omega}_f$ and the corresponding left eigenvector ϕ (i.e., right eigenvector of \mathbf{H}^\dagger), then

$$\mathbf{H}(\Gamma^3 \phi) = \Gamma^3 \mathbf{H}^\dagger \phi = \tilde{\omega}_f^*(\Gamma^3 \phi). \quad (\text{S24})$$

Hence, $\Gamma^3 \phi$ is a (right) eigenvector of \mathbf{H} with eigenvalue $\tilde{\omega}_f^*$.

As noted in the main text, the combination of these two symmetries implies that the eigenvalues form either a complex quadruplet $\{\tilde{\omega}_f, -\tilde{\omega}_f^*, -\tilde{\omega}_f, \tilde{\omega}_f^*\}$ (referred as broken symmetry), or two independent pairs $\{\tilde{\omega}_f, -\tilde{\omega}_f\}$ and $\{\tilde{\omega}'_f, -\tilde{\omega}'_f\}$ which are purely real or purely imaginary (referred as unbroken symmetry), or degenerate zero modes $\tilde{\omega}_f = \tilde{\omega}'_f = 0$.

Another important property of the BdG Hamiltonian is the “non-Hermitian particle/hole pinning” mentioned in the main text. Using Eq. (S16), the BdG eigenproblem can be decomposed into

$$\mathbf{H}_u \mathbf{u} + \mathbf{H}_v \mathbf{v} = \tilde{\omega}_f \mathbf{u} \quad (\text{S25})$$

$$-\mathbf{H}_v^* \mathbf{u} - \mathbf{H}_u \mathbf{v} = \tilde{\omega}_f \mathbf{v}. \quad (\text{S26})$$

By left-multiplying (S25) by \mathbf{u}^\dagger , and right-multiplying the Hermitian conjugate of (S26) by \mathbf{v} , we obtain

$$\mathbf{u}^\dagger \mathbf{H}_u \mathbf{u} + \mathbf{u}^\dagger \mathbf{H}_v \mathbf{v} = \tilde{\omega}_f \mathbf{u}^\dagger \mathbf{u} \quad (\text{S27})$$

$$\mathbf{u}^\dagger \mathbf{H}_v^T \mathbf{v} + \mathbf{v}^\dagger \mathbf{H}_u^\dagger \mathbf{v} = -\tilde{\omega}_f^* \mathbf{v}^\dagger \mathbf{v}. \quad (\text{S28})$$

Using the fact that \mathbf{H}_v is symmetric, we can eliminate the term $\mathbf{u}^\dagger \mathbf{H}_v \mathbf{v}$ and thereby obtain

$$\mathbf{u}^\dagger \mathbf{H}_u \mathbf{u} - \mathbf{v}^\dagger \mathbf{H}_u \mathbf{v} = \tilde{\omega}_f \|\mathbf{u}\|^2 + \tilde{\omega}_f^* \|\mathbf{v}\|^2. \quad (\text{S29})$$

The left side of this equation is evidently real. Therefore, the right side gives

$$(\|\mathbf{u}\|^2 - \|\mathbf{v}\|^2) \text{Im}(\omega_f) = 0. \quad (\text{S30})$$

When pseudo-Hermiticity is unbroken, $\text{Im}(\omega_f) = 0$, Eq. (S30) is satisfied automatically. On the other hand, for an eigenstate that breaks pseudo-Hermiticity, $\text{Im}(\omega_f) \neq 0$, it must be that $\|\mathbf{u}\|^2 = \|\mathbf{v}\|^2$. In the main text, this non-Hermitian particle/hole pinning provides an additional experimental signature for the breaking of pseudo-Hermiticity. Note that the pinning only concerns the total particle/hole populations, which are summed over all lattice sites; the local quantities $|u_n|^2$ and $|v_n|^2$ need not be equal.

DESIGN OF NONLINEAR CIRCUIT LATTICE

Fig. S1 depicts one unit cell of the nonlinear 1D circuit lattice (nonlinear transmission line). It consists of a driven RLC resonator containing a nonlinear capacitance modelled by

$$C_{NL}(V) = \frac{dQ}{dV} = C_0 + C_1 V^2. \quad (\text{S31})$$

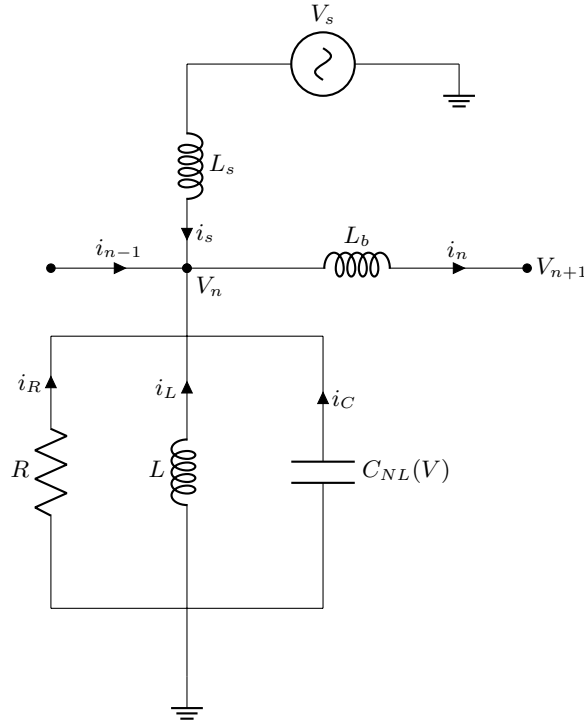


FIG. S1. The unit cell of a nonlinear capacitor circuit that can cause Bogoliubov fluctuations.

By Kirchhoff's law of current conservation, the various AC currents in the unit cell obey

$$i_{n-1} + i_s + i_R + i_L + i_C - i_n = 0. \quad (\text{S32})$$

The time derivatives of the current through the inductors obey

$$\dot{i}_s = \frac{1}{L_s}(V_s - V_n), \quad (\text{S33})$$

$$\dot{i}_L = -\frac{1}{L}V_n, \quad (\text{S34})$$

$$\dot{i}_n = \frac{1}{L_b}(V_n - V_{n+1}), \quad (\text{S35})$$

$$\dot{i}_{n-1} = \frac{1}{L_b}(V_{n-1} - V_n). \quad (\text{S36})$$

Similarly, the time derivative of the current through the nonlinear capacitor obeys

$$Q_C \int_0^{V_n} C_{NL} dV, \quad (\text{S37})$$

$$\Rightarrow i_C = \dot{V}_n \cdot C_{NL} = C_0 \dot{V}_n + C_1 \dot{V}_n V_n^2, \quad (\text{S38})$$

$$\Rightarrow \dot{i}_C = C_0 \ddot{V}_n + C_1 \ddot{V}_n V_n^2 + 2C_1 \dot{V}_n^2 V_n. \quad (\text{S39})$$

And for the resistor,

$$i_R = \frac{V_n}{R}, \quad (\text{S40})$$

$$\Rightarrow \dot{i}_R = \frac{\dot{V}_n}{R}. \quad (\text{S41})$$

Combining all the above equations, we arrive at the equation of motion

$$C_0 \ddot{V}_n + \frac{\dot{V}_n}{R} + \left(\frac{1}{L_s} + \frac{2}{L_b} + \frac{1}{L} \right) V_n + C_1 \ddot{V}_n V_n^2 + 2C_1 \dot{V}_n^2 V_n + \frac{2}{L_b} \bar{V}_n + \frac{V_s}{L_s} = 0, \quad (\text{S42})$$

where

$$\bar{V}_n \equiv \frac{1}{2}(V_{n+1} + V_{n-1}). \quad (\text{S43})$$

Next, we wish to show that this equation of motion can be analyzed using a BdG transformation, similar to the preceding toy model. Let us assume the driving voltage has the form

$$V_s = \frac{1}{2} (V e^{-i\omega_p t} + \text{c.c.}), \quad (\text{S44})$$

where c.c. stands for "complex conjugate". We take the following ansatz:

$$V_n = \frac{1}{2} (\Psi_n e^{-i\omega_p t} + \text{c.c.}), \quad (\text{S45})$$

$$\Rightarrow \dot{V}_n = \frac{1}{2} \left(-i\omega_p \Psi_n e^{-i\omega_p t} + \dot{\Psi}_n e^{-i\omega_p t} + \text{c.c.} \right), \quad (\text{S46})$$

$$\Rightarrow \ddot{V}_n = \frac{1}{2} \left(-\omega_p^2 \Psi_n e^{-i\omega_p t} - 2i\omega_p \dot{\Psi}_n e^{-i\omega_p t} + \ddot{\Psi}_n e^{-i\omega_p t} + \text{c.c.} \right). \quad (\text{S47})$$

We now make two simplifying approximations:

1. We assume the nonlinearity in the circuit is weak, and that a small perturbation is applied after the system has reached its steady state, producing a small fluctuation on top of the steady state with frequency much lower than the driving frequency. This is the slowly-varying envelope approximation (SVEA) [43]. Hence, we drop terms involving $\ddot{\Psi}_n$, $|\dot{\Psi}_n|^2$, $\dot{\Psi}_n^2$, etc.

2. We keep only terms with angular frequencies around ω_p , as higher-frequency oscillations average to zero. However, we have to be careful about how terms are dropped. Terms that oscillate as $e^{2i\omega_p t}$ or $e^{-2i\omega_p t}$ can only be discarded at the final step, but not at intermediate steps, since the nonlinearity can allow them to combine with their complex conjugate counterparts to produce lower-frequency terms.

With these two approximations, the two nonlinear terms in Eq. (S42) become

$$\dot{V}_n V_n^2 + 2\dot{V}_n^2 V_n \approx \frac{1}{8} \left[- \left(\omega_p^2 |\Psi_n|^2 \Psi_n + 2i\omega_p \dot{\Psi}_n^* \Psi_n^2 + 4i\omega_p |\Psi_n|^2 \dot{\Psi}_n \right) e^{-i\omega_p t} + \text{c.c.} \right]. \quad (\text{S48})$$

Note the presence of the term $\dot{\Psi}_n^*$, which involves the complex conjugate of V_n . Substituting this back into (7) and collecting terms appropriately, we obtain

$$\left(-2i\omega_p C_0 + \frac{1}{R} \right) \dot{\Psi}_n + \left[C_0(\omega_0^2 - \omega_p^2) + \frac{i\omega_p}{R} \right] \Psi_n - \frac{1}{4} C_1 \omega_p^2 |\Psi_n|^2 \Psi_n - \frac{1}{2} i C_1 \omega_p \dot{\Psi}_n^* \Psi_n^2 - i C_1 \omega_p |\Psi_n|^2 \dot{\Psi}_n + \frac{2}{L_b} \bar{\Psi}_n + \frac{V}{L_s} = 0, \quad (\text{S49})$$

where

$$\omega_0 = \sqrt{\frac{1}{C_0} \left(\frac{1}{L_s} + \frac{2}{L_b} + \frac{1}{L} \right)} \quad (\text{S50})$$

is the natural frequency.

We are now ready to apply the Bogoliubov ansatz. The procedure is similar to the toy model described in the previous section. Let us define

$$\Psi_n = \psi_n + u_n e^{-i\omega_f t} + v_n^* e^{i\omega_f^* t}, \quad (\text{S51})$$

$$\Rightarrow \dot{\Psi}_n = -i\omega_f u_n e^{-i\omega_f t} + i\omega_f^* v_n^* e^{i\omega_f^* t}. \quad (\text{S52})$$

Here, the Bogoliubov fluctuations are described by the envelope functions $u_n e^{-i\omega_f t}$ and $v_n^* e^{i\omega_f^* t}$, whereas ψ_n represents the steady-state amplitude. For self-consistency, the amplitude and frequency of the fluctuations should be much less than the steady amplitude and driving frequency, respectively. Accordingly, we discard higher-order terms like $|u_n|^2$ and $|v_n|^2$, resulting in

$$|\Psi_n|^2 \Psi_n \approx |\psi_n|^2 \psi_n + (\psi_n^2 v_n + 2|\psi_n|^2 u_n) e^{-i\omega_f t} + (\psi_n^2 u_n^* + 2|\psi_n|^2 v_n^*) e^{i\omega_f^* t}, \quad (\text{S53})$$

$$\Psi_n^2 \dot{\Psi}_n^* \approx -i\omega_f \psi_n^2 v_n e^{-i\omega_f t} + i\omega_f^* \psi_n^2 u_n^* e^{i\omega_f^* t}, \quad (\text{S54})$$

$$|\Psi_n|^2 \dot{\Psi}_n \approx -i\omega_f |\psi_n|^2 u_n e^{-i\omega_f t} + i\omega_f^* |\psi_n|^2 v_n^* e^{i\omega_f^* t}. \quad (\text{S55})$$

Substituting back into Eq. (S49) and taking the coefficients of the steady state, we obtain

$$\left[C_0(\omega_0^2 - \omega_p^2) + \frac{i\omega_p}{R} \right] \psi_n - \frac{1}{4} C_1 \omega_p^2 |\psi_n|^2 \psi_n + \frac{2}{L_b} \bar{\psi}_n + \frac{V}{L_s} = 0. \quad (\text{S56})$$

This describes the steady state amplitude, so it is reasonable that the expression does not involve u_n and v_n . Likewise, we can extract the equations for $e^{-i\omega_f t}$ and $e^{i\omega_f^* t}$ respectively (for the latter, we simply take the complex conjugates):

$$\left[C_0(\omega_0^2 - \omega_p^2) + \frac{i\omega_p}{R} \right] u_n + \left(-2C_0\omega_p - \frac{i}{R} \right) \omega_f u_n - \frac{1}{4} C_1 \omega_p^2 (\psi_n^2 v_n + 2|\psi_n|^2 u_n) - \frac{1}{2} C_1 \omega_p \omega_f \psi_n^2 v_n - C_1 \omega_p \omega_f |\psi_n|^2 u_n + \frac{2}{L_b} \bar{u}_n = 0, \quad (\text{S57})$$

$$\left[C_0(\omega_0^2 - \omega_p^2) - \frac{i\omega_p}{R} \right] v_n - \left(-2C_0\omega_p + \frac{i}{R} \right) \omega_f v_n - \frac{1}{4} C_1 \omega_p^2 (\psi_n^{*2} u_n + 2|\psi_n|^2 v_n) + \frac{1}{2} C_1 \omega_p \omega_f \psi_n^{*2} u_n + C_1 \omega_p \omega_f |\psi_n|^2 v_n - \frac{2}{L_b} \bar{v}_n = 0. \quad (\text{S58})$$

We can then rearrange Eqs. (S57)–(S58) into the form

$$\left[\begin{pmatrix} \mathbf{H}_u & \mathbf{H}_v \\ -\mathbf{H}_v^* & -\mathbf{H}_u \end{pmatrix} + i\Gamma \mathbf{I} \right] \begin{pmatrix} \mathbf{u} \\ \mathbf{v} \end{pmatrix} = \begin{pmatrix} \omega_f \\ \omega_p \end{pmatrix} \begin{pmatrix} \mathbf{G}_u & \mathbf{G}_v \\ \mathbf{G}_v^* & \mathbf{G}_u^* \end{pmatrix} \begin{pmatrix} \mathbf{u} \\ \mathbf{v} \end{pmatrix}, \quad (\text{S59})$$

where

$$(\mathbf{H}_u)_{nn} = \frac{1}{2} \left(\frac{\omega_0}{\omega_p} - \frac{\omega_p}{\omega_0} \right) - \frac{g}{2} \frac{\omega_p}{\omega_0} |\psi_n|^2, \quad (\text{S60})$$

$$(\mathbf{H}_u)_{n(n+1)} = (\mathbf{H}_u)_{(n+1)n} = \frac{1}{2L_b C_0 \omega_0 \omega_p}, \quad (\text{S61})$$

$$(\mathbf{H}_v)_{nn} = -\frac{g}{2} \frac{\omega_p}{\omega_0} \psi_n^2, \quad (\text{S62})$$

$$(\mathbf{G}_u)_{nn} = \frac{\omega_p}{\omega_0} + g \frac{\omega_p}{\omega_0} |\psi_n|^2 + i\Gamma, \quad (\text{S63})$$

$$(\mathbf{G}_v)_{nn} = \frac{g}{2} \frac{\omega_p}{\omega_0} \psi_n^2, \quad (\text{S64})$$

Here, M_{ij} denotes the matrix element in the i -th row and j -th column. All other matrix elements are zero. We have introduced the dimensionless parameters

$$\Gamma = \frac{1}{2RC_0\omega_0} \quad (\text{S65})$$

$$g = \frac{C_1}{2C_0}. \quad (\text{S66})$$

Eq. (S59) is a generalized eigenproblem, rather than an ordinary eigenproblem, due to the presence of the matrix \mathbf{G} on the right-hand side. Based on the generalized eigenvalue ω_f/ω_p , we define

$$\Omega_f = \frac{\omega_f}{\omega_p} + i\Gamma, \quad (\text{S67})$$

which we interpret as the dimensionless ‘‘BdG eigenfrequency’’. As noted in the main text, this implies that the corresponding dimensionful physical frequency associated with this fluctuation mode is $(\Omega_f - i\Gamma)\omega_p$.

The above procedure applies equally well to Bloch modes in the PBC problem. In a spatially infinite lattice, we can apply a spatial Fourier transform to u_n and v_n . The generalized eigenvalue problem (S59) then simplifies to a Bloch form with \mathbf{H} replaced by a Bloch Hamiltonian \mathbf{H}_k .

There is one notable issue with the \mathbf{G} matrix on the right-hand side of Eq. (S59): it explicitly breaks pseudo-Hermiticity and non-Hermitian particle-hole symmetry for the generalized eigenproblem, despite the \mathbf{H} matrix possessing those symmetries. (The Bloch/PBC version of the problem is similarly affected.) If we re-trace the origins of \mathbf{G} , we find that it is tied to the fact that the voltage variable V_n is real, unlike the complex wavefunction Ψ_σ in the toy model, and this generates extra terms via the nonlinearity.

However, this complication does not qualitatively alter the behavior or implications of the model. In Fig. S2, we plot the BdG eigenfrequencies for the Bloch (PBC) lattice. The red dashes are obtained using the full \mathbf{G} matrix, while the green solid lines show the results with \mathbf{G} replaced by the constant

$$G = \frac{\omega_p}{\omega_0} + i\Gamma \quad (\text{S68})$$

(i.e., the nonlinear part of the diagonal block \mathbf{G}_u and the off-diagonal block \mathbf{G}_v are omitted). We use this approximation when plotting the theoretical spectra in Fig. 2 and Fig. 3(d) of the main text. As shown by Fig. S2, using the full \mathbf{G} matrix would give similar outcomes; for example, in the range of k corresponding to unbroken pseudo-Hermiticity, the Ω_f 's would have very small imaginary parts rather than being exactly real.

FABRICATION AND CHARACTERIZATION OF CIRCUIT

The PCB was assembled by Seed Studio, using the circuit components listed in Table S1. The table also lists the vendor-supplied circuit component parameters, which are used to calculate the spectra in Fig. 2 and Fig. 3(d) of the main text, as well as Fig. S2.

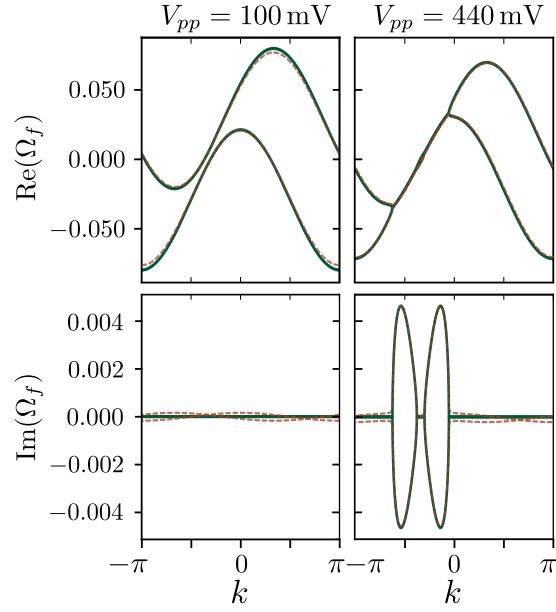


FIG. S2. PBC spectrum with the full \mathbf{G} matrix (red dashes), and with \mathbf{G} replaced by a constant (green solid lines). All parameters are the same as in the right panel of Fig. 2(b) in the main text.

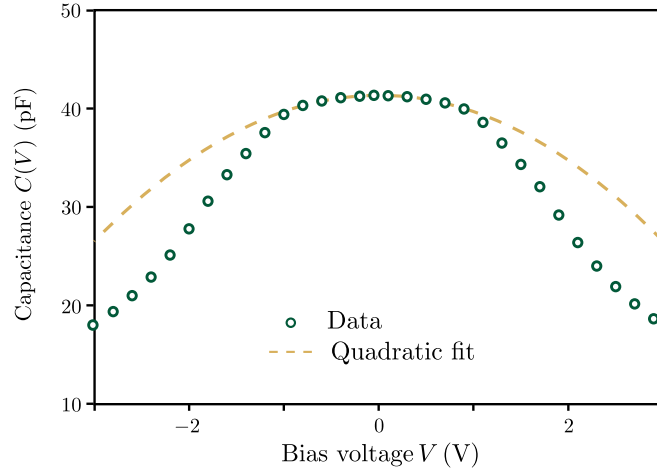


FIG. S3. Capacitance of back-to-back varactors, based on the vendor datasheet (yellow dashes) and the quadratic approximation in Table S1 (green circles).

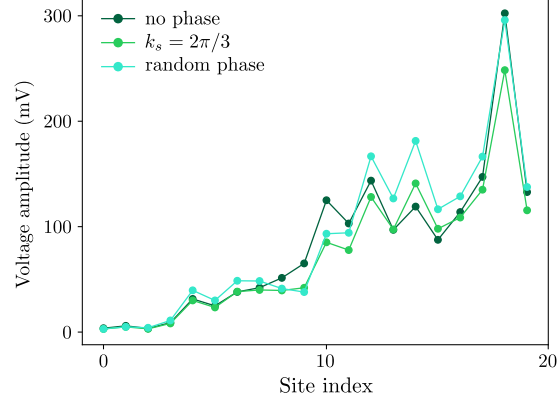
The circuit is driven by a Tektronix AWG70002A Arbitrary Waveform Generator and AFG31000 Arbitrary Function Generator, with built-in synchronization function sync the phases of input signals. The signals are recorded by a Tektronix DPO73304DX Digital Phosphor Oscilloscope.

The nonlinear capacitances in the transmission line are implemented using back-to-back varactors [43, 44]. The quadratic expression for $C(V)$ stated in Table S1 is obtained by fitting, using the nonlinear voltage response from the vendor datasheet. As shown in Fig. S3, this quadratic expression closely matches the full nonlinear capacitance for $V \lesssim 1$ V, which is well within the operating regime for our experiment.

As the Bogoliubov modes are lossy, we activate them with an auxiliary drive. In the experiment, we choose to apply this auxiliary drive uniformly on every site. However, the results we obtain, including the observations of the NHSE, are relatively insensitive to the spatial distribution of the auxiliary drive. For instance, Fig. S4 shows numerical (SPICE) simulation results for three different auxiliary drive settings: equal phase (as in the experiment), a fixed phase shift of $2\pi/3$ on successive sites, and random phases on every site. In all cases, the sideband amplitude distributions clearly exhibit the NHSE.

Component	Symbol	Value	Part number
back-to-back varactors	$C_0 + C_1 V^2$	$41.344 - 1.649V^2$ pF	SMV1255-011LF
onsite inductance	L	$100 \mu\text{H}$	8250-101K-RC
source inductance	L_s	$100 \mu\text{H}$	8250-101K-RC
binding inductance	L_b	$1000 \mu\text{H}$	8250-102K-RC
onsite resistance	R	$150 \text{k}\Omega$	PR03000401503JPC00

TABLE S1. Circuit parameters and part numbers used in the experiment.

FIG. S4. SPICE simulations of the circuit with different choices of auxiliary drive phase distribution: equal phases on every site, a $2\pi/3$ phase shift on successive sites, and random phases. All circuit components are the same as in Table. S1.